PAPER

Check for updates

In situ synthesis of holey g-C₃N₄ nanosheets decorated by hydroxyapatite nanospheres as efficient visible light photocatalyst†

Mohammad Chahkandi, [ID] *[a] Mahboobeh Zargazi,*[b] Afsaneh Ahmadi,[a] Ehsan Koushki [ID] [c] and Arman Ghasedi [ID] [c]

The interesting g-C₃N₄ nanosheet morphology has drawn huge attention in photocatalytic applications because of its special features. Nonetheless, the relative activity of these nanosheets is still controversial due to the low available active sites and the high recombination probability of photo-induced charge carriers. In this work, in situ sol–gel approach was applied to synthesize holey g-C₃N₄ nanosheets/ hydroxyapatite (HAp) nanospheres with plentiful in-plane holes. Herein, the presence of Ca^{2+} plays a key role in the formation of holey defects on 2D g-C₃N₄. In-plane holes provide nanosheets with more active edges and diffusion channelsv, resulting in a tremendous enhanced mass and photo-induced charge transfer speed. Moreover, the holes make highly numbered boundaries, which lead to the prevention of aggregation. On the other hand, distributed nano-HAp spheres on these nanosheets can form effective heterojunctions having high photo-degradation ability of pollutants. Intrinsic O-vacancies inside HAp unit cells mainly affect the capture of photogenerated electrons, pollutant molecules, and O_2 gas. The synergistic presence of O-vacancies and holey defects (C-vacancies) on 2D g-C₃N₄ plays a key role in raising the photocatalytic performance of holey g-C₃N₄/HAp. It can be concluded that the proposed preparation method is a promising approach for simultaneous synthesis of holey g-C₃N₄ and surface heterojunctions of Ca-based materials. This new structure has shown significant degradation ability of bisphenol A, a prominent pollutant, with a low amount (0.01 g) and short time.

1. Introduction

Technology and industries in the modern world have rapidly grown to facilitate human life, such as the construction of advanced machines and employing nano fabrications in various fields (medicine, genetics, and so on).[1,2] Despite the benefits, they have also caused irreparable damage to the environment and ultimately to human health. The fast flux of dangerous contaminants to the ground and surface water with the malicious footprints in ecosystems are worrying.[3,4] For many years, researchers have pursued simple but still effective ways to reduce or eliminate these pollutants from aquatic environments.[5,6] Among the techniques, the photocatalytic process has

attracted more attention due to the simple, low cost (from the view of energy source), and supreme performance without the liberation of any secondary pollutants compared to the conventional methods (adsorption, ozonation, and ion exchange).[7,8] Recently, because of diminishing photocatalytic activities, researchers have switched their routes to the synthesis of nanocomposites or immobilized forms on supports.[9,11–13] Immobilized photocatalysts could improve charge separation and enhance degradation performance. Considering this effective remediation method, graphitic carbon nitride (g-C₃N₄) was introduced in 2009 as an excellent photocatalyst with eco-friendly characteristics, nontoxicity, thermal and chemical stability, low-cost preparation, and easy cut-rate fabrication.[14,15] Nevertheless, low surface area, unsatisfactory high visible-light absorption, and fast recombination rate of photogenerated charges from the π–π system (triazine rings) severely restrict the photocatalytic activity of pristine bulk g-C₃N₄. Hitherto, two main classified strategies were proposed to resolve the g-C₃N₄ deficiencies considering the band gap and structural engineering.[16] The former factor can be obtained by insertion and/or doping functional elements, modification using heteroatoms, and making heterojunction semiconductors.[17,18] The latter method provides various morphological structures of g-C₃N₄ such as nanosheets,[19] nanorods,[20]

[a]Department of Chemistry, Hakim Sabzevari University, Sabzevar 96179-76487, Iran. E-mail: m.chahkandi@hsu.ac.ir; Fax: +985144012451; Tel: +985144013342

[b]Department of Chemistry, Faculty of Science, Ferdowsi University of Mashhad, Mashhad, 91775, Iran

[c]Department of Physics, Hakim Sabzevari University, Sabzevar 96179-76487, Iran

† Electronic supplementary information (ESI) available: Includes the isoelectric point of HAp/g-C₃N₄; photodegradation BPA efficiency for various ratios of HAp and g-C₃N₄ components; photocatalytic degradation in the presence of trapping agents; re-cycling studies for photocatalytic process; photocatalytic efficiency for other pollutants; and XPS spectra for the nanocomposite before and after the photocatalytic process. See DOI: 10.1039/d1ra05259d

nanotubes,[15] and so on with remarkable physicochemical features. Especially, 2D nanosheets of g-C3N4 have attracted much attention due to their high surface area, enhanced electron–phonon interactions, and vast in-plane electron mobility.[21] Nevertheless, the available active sites on the nanosheet surface are still confined due to boundaries and edges. The delocalized electron density of triazine rings makes π–π stacking forces to array those ordered nanosheets averting the aggregation and also prevent the transportation of the formed H_2O_2 intermediates, which results in poisoning g-C3N4 nanosheets, leading to limited photocatalytic performance. The highlighted drawbacks can be remarkably diminished by the creation of porous sites in g-C3N4 nanosheets. Recently, high photocatalytic performance has been demonstrated within the fabrication of 3D g-C3N4 with porous sheets.[22] The in-plane pores dispersed all over the holey g-C3N4 nanosheets can improve mass and charge transport along the sheets. On the other hand, holes prevent sheet aggregation because of possessing of interstice interaction sites. Despite the numerous investigations about the synthesis of g-C3N4 nanosheets, preparation of its composites with holey nanosheet morphology is still a controversial challenge. Liang et al. reported a thermal treatment synthetic method for this morphological structure under ammonia gas with great photocatalytic performance for hydrogen evolution compared to the conventional g-C3N4.[23] An effective photocatalyst of oxygen edged holey g-C3N4 nanosheets was constructed under photo-Fenton-reaction and UV irradiation with remarkable pollutant degradation.[24,25] Moreover, porous holey nanosheets were synthesized via the pre-polymerization method showing high photocatalytic H_2 evolution under ammonia gas pressure.[26] Also, similar works for the preparation of the mentioned morphologies suffer from complex processes and are time-consuming.[27,28] However, herein, an effective strategy was applied for simple and cost-effective sol–gel-derived holey g-C3N4 nanosheets decorated by HAp NPs.

Recently, the photocatalytic activity of HAp in different forms was investigated. Biphasic HAp–titana indicated high photocatalytic performance compared to the single phase titana or HAp and also Ti-doped form of HAp. However, some single forms of HAp without any dopant have photocatalytic efficiency in the degradation of methyl mercaptan and dimethyl sulphate.[29]

Z-scan method is a well-known technique for measurements of nonlinear refractive and absorption coefficients because of its accuracy and simplicity.[30] In this method, through movement of the sample along the z-axis (horizontal direction shown in Scheme 1) nonlinear absorption coefficient and refractive index of the sample are obtained by open and close aperture

experiments, respectively. Nonlinear refraction could be due to thermal lensing, electron transition attributed to third order nonlinearity (Kerr effect), and optical reorientation effect.[31] Electrical nonlinear refraction is a weak phenomenon in low laser illuminations and could be negligible. Z-scan experiments give useful information about the nonlinear optical coefficients of materials in interaction with different laser beam intensities. NPs have been extensively used in optical and electrical applications due to their unique electronic and quantum structures and also thermal and chemical stability. High photoluminescence efficiency, photovoltaic property, and plasmonic resonance of NPs have been widely considered in optical applications.[31–33] Nonlinear optical properties of NPs are studied due to their unique characteristics, such as saturation absorption,[34] optical Kerr effect,[35] and reorientation effect.[36] Materials with low threshold saturation intensity are proposed in controllable transparent media, light amplifier mediums, laser cavities, and Q-switching devices.[37]

In the present work, we introduced a novel facile sol–gel-derived heterojunction of holey g-C3N4 nanosheets/HAp. The structure includes HAp NPs decorated on the holey sites of in situ fabricated g-C3N4 nanosheets. Compared with pure HAp and g-C3N4, the prepared composite demonstrated significantly improved photocatalytic capability for bisphenol A (BPA) degradation under visible-light illumination. This activity can be attributed to the numerous holes dispersed on the in-planes of g-C3N4. Moreover, the obtained results of z-scan experiments for the appropriate NPs show the low threshold saturable intensity for the colloidal solution of these particles, which confirms its potential implementation in the optical devices.

2. Experimental

2.1. Materials

Calcium nitrate $Ca(NO_3)_2 \cdot 4H_2O$, melamine ($C_3H_6N_6$), sodium dihydrogen phosphate (NaH_2PO_4), and bisphenol A ($C_{15}H_{16}O_2$) were purchased from Merck Company. Tri-ethyl phosphate (TEP; $(C_2H_5)_3PO_4$) was also purchased from FLUKA. All materials were used without further purification.

2.2. Synthesis of photocatalyst

2.2.1. Sol–gel synthesis of HAp. Solution A: 0.012 mole of TEP was dissolved in 14 ml distilled water, and then, a small amount of ethanol was added. The resulting solution was hydrolyzed under stirring at 35 °C for 23 h. Solution B: 0.02 mole calcium nitrate was dissolved in distilled water under stirring for 30 min. Solution A was dropwise added to solution B
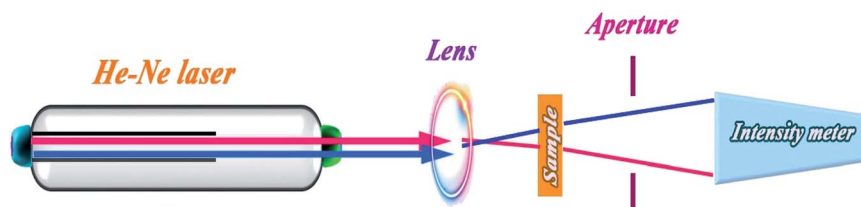
Scheme 1 Schematic z-scan setup shows the movement of sample along the z-axis.

under stirring. Then, the solution pH was fixed at 10 using NaOH (1 M). The resulting clear sol was stirred vigorously for 1 h at room temperature. Sol was aged for 5 days and then heated at 60 °C for 24 h to form a white dried gel. Finally, it was calcined at 600 °C with a rate of 2° min⁻¹.

2.2.2. Synthesis of g-C₃N₄. Graphitic carbon nitride was synthesized by a simple thermal method. A specific amount of melamine was dried at 120 °C in an oven. 5 g of dried melamine powder was placed in a crucible with a cap and heated at 600 °C with 2° min⁻¹ for 2 h, yielding a final yellowish powder.

2.2.3. Synthesis of nanocomposite (HAp/g-C₃N₄). Various nanocomposites of HAp/g-C₃N₄ with 80 : 20, 70 : 30, 60 : 40, and 50 : 50 ratios were synthesized *via* a facile sol–gel method as described below: first, the mixture sol of solutions A and B was prepared similar to the above-mentioned synthesis procedure of HAp. Then, after adding an aqueous solution of TEP, appropriate amounts of melamine for every mentioned ratio of HAp to g-C₃N₄ were added to the sol suspension and continuously stirred for 1 h. The obtained sols were aged, dried, and calcined at 600 °C for 2 h in a closed crucible. Resultant powder samples were washed with distilled water and absolute ethanol several times. More details are depicted in Scheme 2. The exhaust of nitrogen gas because of HAp calcination led to the exfoliation of g-C₃N₄ nanosheet from its bulk form.

2.3. Characterization of photocatalyst

Crystalline structures of samples were determined by X-ray diffraction (XRD) (Explorer GNR Italia at 40 kV and 30 mA with CuKα radiation (λ = 1.5418 Å)). Samples were also evaluated by Fourier transmittance infrared (FT-IR) spectroscopy using Shimadzu FT-IR 8400S spectrometer (KBr) in the range of 500–4000 cm⁻¹. Morphology and shape of photocatalysts were observed using field emission scanning electron microscopy (FE-SEM) by (SEM; LEO-Germany). The elemental composition of photocatalysts was also investigated by energy X-ray dispersive spectroscopy (EDS) attached to the SEM apparatus. Morphology of the nanocomposite was detected by transmittance electron microscopy (TEM-FM 208S-USA). X-ray photoelectron spectroscopy (XPS) was applied for g-C₃N₄ and HAp/g-C₃N₄ by an AvaSpec-ULS-TEC (Poland) system. The specific surface area of all compounds was measured by an appropriate instrument (BET, Quantachrome Instruments, USA) based on Brunauer–Emmett–Teller (BET) method. Photoluminescence (PL-AVATAR-USA) was applied for the determination of the hole–electron pairs photogenerated on the photocatalyst surface. Mott–Schottky (M–S) measurement was done *via* a routine three-electrode system (counter: Pt; reference: standard calomel in saturated KCl; working: glassy carbon) controlled with a computer of potentiostat/galvanostat (METROHM AUTOLAB 201). The performance of photoelectron chemical cell of all samples (HAp, g-C₃N₄, and HAp/g-C₃N₄) was executed in a quartz cell filled with 0.5 M Na₂SO₄ electrolyte at a potential ranging from −0.1 to 1.5 V with Ag/AgCl as reference electrode under 1000 Hz frequency.

2.4. Photocatalytic evaluation

Photocatalytic activity of nanocomposites was evaluated by photodegradation of BPA (10 ppm, 10 ml) in an aqueous
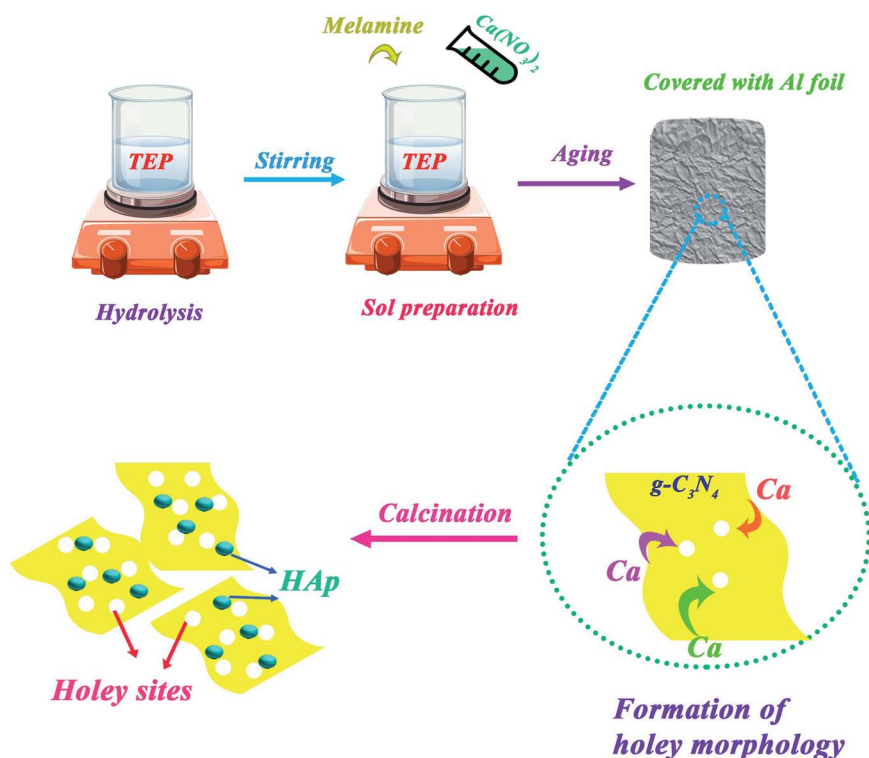
Scheme 2 Synthetic process of HAp/g-C₃N₄ nanocomposite.

solution. First, the photocatalyst and pollutant were inserted in the dark to reach adsorption–desorption equilibrium for 90 min. The photocatalytic activity was evaluated by subjecting the suspension to an LED lamp (IP 65, 200 W) as the light source. After specific interval times, the sample was centrifuged, and the concentration of BPA by UV-visible spectroscopy (EU-2200) at a characterized wavelength (665 nm) was measured. To gain high photocatalytic efficiency, the related parameters were optimized for the photocatalytic process. These parameters include photocatalyst amount, pH, and BPA concentration. For a comparative evaluation of the photocatalytic activity of the nanocomposite, the photocatalytic process was also conducted for single phases of HAp and g-C_3N_4.

2.5. Optical procedure

In z-scan experiment, a laser beam is focused using a lens, and the sample scans the focused beam. As the sample approaches the focal point, the beam intensity increases, and the optical indices change. The change in the refractive index shows itself in diverging (for samples with nonlinear refractive index $n < 20$) or converging ($n > 20$) of the beam. It changes the power of the passing beam through a close circular aperture. The obtained data of the passing power *versus* the sample position (z) is called the close-aperture z-scan curve. If the aperture is removed and the total transmitted power is measured, the effect of absorption only can be detected in the detector, and the resultant curve is named open-aperture z-scan curve.

3. Results and discussion

3.1. Nanocomposite (HAp/g-C_3N_4) characterization

XRD patterns indicated the crystallinity and phase of HAp/g-C_3N_4(50 : 50), HAp, and g-C_3N_4 (Fig. 1a). Diffraction peaks of g-C_3N_4 sample are attributed to pure g-C_3N_4 phase (JCPDS card no. 87-1526) with a strong characteristic peak at $2\theta = 27.4°$ having hexagonal unit cell. Moreover, all recorded diffracted peaks of HAp at $2\theta = 26°$ (002), 32° (112), 34° (202), 37° (310),

47° (222) well indexed to its hexagonal structural unit cell (JCPDS card no. 9-0432). However, the diffraction pattern of the HAp/g-C_3N_4 nanocomposite shows a mixture of all peaks of single phases but with some shift to lower degrees and losing the crystallinity toward an amorphous composite, but can be assigned to two individual contents (HAp and g-C_3N_4) without the formation of any secondary phase. The diffraction peak of {002} *hkl* plane of g-C_3N_4 in the nanocomposite has shifted to a higher degree along with the decreased intensity due to the formation of holes in g-C_3N_4 nanosheets.[23]

Fig. 1b shows the FT-IR spectra for HAp, g-C_3N_4, and HAp/g-C_3N_4 nanocomposite. The characteristic peaks of PO_4^{3-} group of HAp in wavenumbers of 567, 1041, and 1097 cm^{-1} can be assigned to the bending and stretching modes (asymmetric and symmetric) of the P–O bond, respectively (see Fig. 1b).[38,39] For g-C_3N_4, several peaks at 812, 1241, and 1641 cm^{-1} were observed, which can be attributed to the successful synthesis of g-C_3N_4. In the case of HAp/g-C_3N_4 nanocomposite, the main characteristic bands of both compounds, HAp and g-C_3N_4, can be observed (refer to Fig. 1b). HAp/g-C_3N_4 and single phase of g-C_3N_4 sheet show peak at 3300 cm^{-1} and the broader peak for the single phase g-C_3N_4 can be related to more nitrogen bonding due to enhanced N content. Morphology and shapes of as-prepared samples were evaluated by FE-SEM, which are shown in Fig. 2a–c. This new observed nano-morphology should be compared with the recently reported one. Xu *et al.* have reported a stable structure of g-C_3N_4/HAp with an inverse micro-morphology, in which the microsphere of HAp was decorated by particles of g-C_3N_4 with a considerable agglomeration of HAp spheres, reducing the specific surface area. Fig. 2a depicted the morphology of HAp, showing spherical nanoparticles ranging in size between 15–50 nm with almost homogenous size distribution. Fig. 2b also indicated the layered structures of g-C_3N_4, including the assembled sheets with nanosize thickness (for example: 88.75 nm). Morphology of the nanocomposite HAp/g-C_3N_4 (50 : 50) shows the distributed holey structures on g-C_3N_4 nanosheets in the presence of HAp nanospheres (see Fig. 2c). The inset figure in Fig. 2c indicates defect sites, which
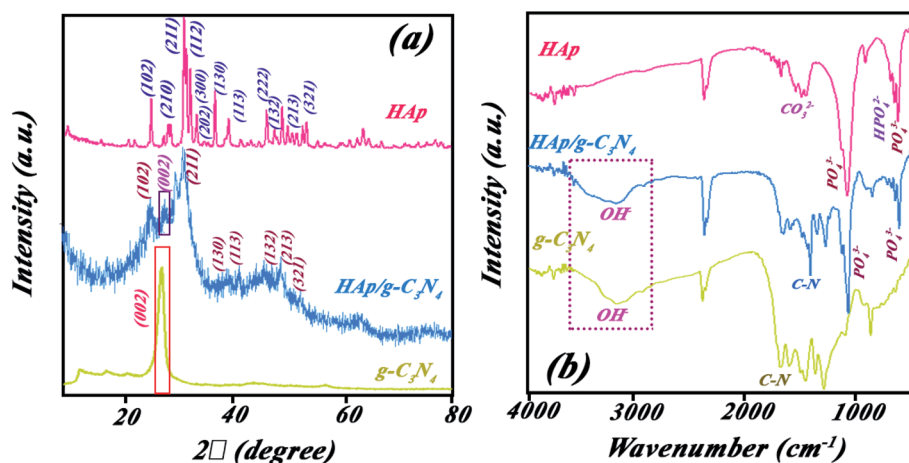

Fig. 1 (a) XRD patterns for HAp/g-C_3N_4, HAp, and g-C_3N_4 samples and inset figure shows high resolution of nanocomposite pattern and (b) FT-IR spectra for HAp-g-C_3N_4, HAp, and g-C_3N_4.
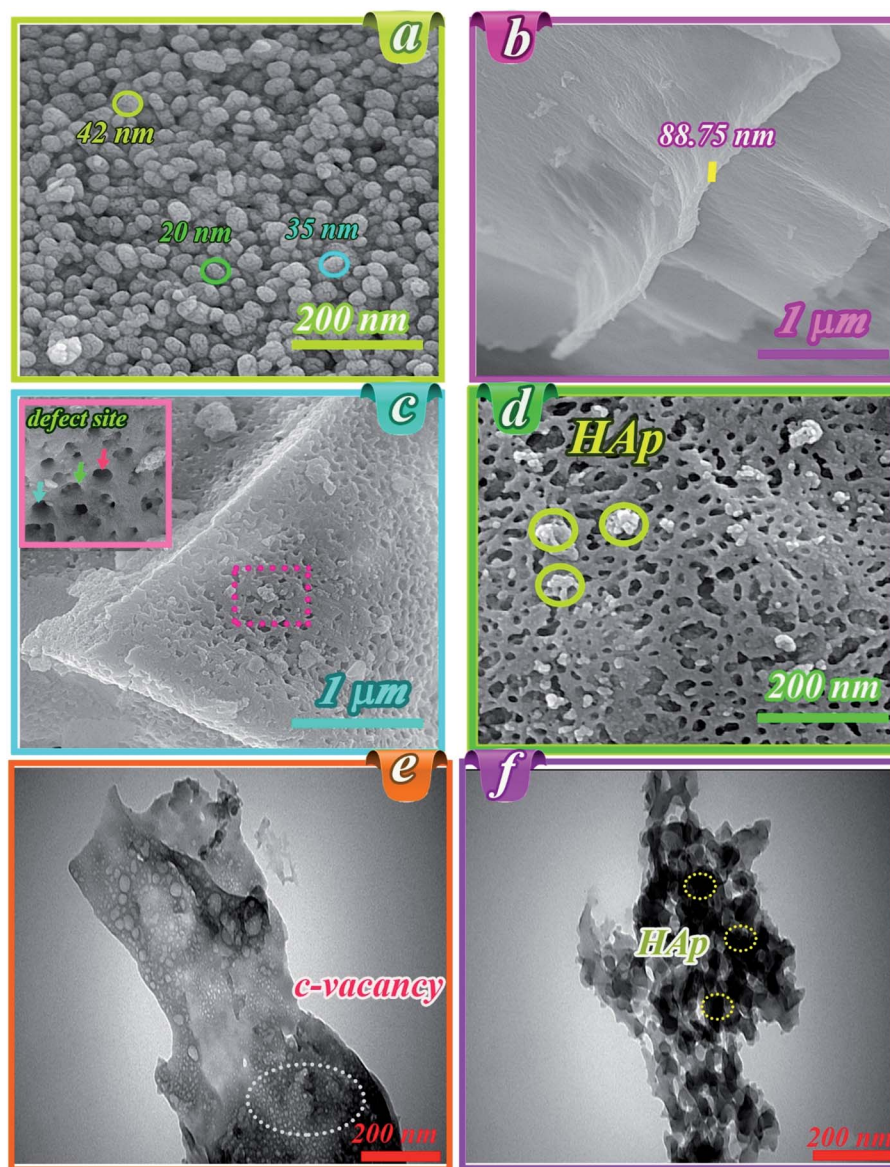
Fig. 2 FE-SEM images for HAp nanospheres (a), g-C$_3$N$_4$ nanosheets (b), HAp/g-C$_3$N$_4$ nanocomposite with distributed defect sites on nanosheets (c), holy structured of g-C$_3$N$_4$ nanosheets including accumulated HAp nanospheres (d), and TEM images for, in-plane hole sites (small white points) indicating C-vacancies over nanosheets (e), and distributed HAp particles over holey structures of g-C$_3$N$_4$ nanosheets (f).

originated from C-vacancies on nanosheets. Various holes with different sizes were formed on nanosheet surfaces (see Fig. 2d). White accumulated nanospheres coated on nanosheets correspond to HAp. TEM images of holey nanosheets are indicated in Fig. 2e, which clearly shows the in-plane hole sites by small white points. Indeed, these white points could be assigned to the C-vacancies in g-C$_3$N$_4$ nanosheets. Fig. 2f depicts the TEM image for the nanocomposite consisting of holey structures of g-C$_3$N$_4$ nanosheets and distributed HAp nanospheres on its surface. EPR curve confirmed the presence of simultaneous C and O vacancies in the HAp/g-C$_3$N$_4$ nanocomposite (Fig. 1S, ESI file†).

The elemental composition of the nanocomposite is indicated in Fig. 3a by EDS spectra. The peaks observed in the EDS spectra were attributed to Ca, P, N, C, and O. Approximate percentage of elements in the nanocomposite was also evaluated by mapping studies (see Fig. 3b–g). Results of mapping analysis confirmed the successful synthesis method for HAp/g-C$_3$N$_4$. Based on BET analysis, it can be highlighted that a permanent spread specific surface area of HAp/g-C$_3$N$_4$ nanocomposite (205 m^2 g^{-1}) and holey morphological structured g-C$_3$N$_4$ nano-sheets (86 m^2 g^{-1}) in comparison with HAp nanospheres (24.5 m^2 g^{-1}) were determined (see Fig. 4). To investigate the pore structure, pore size distributions of samples were obtained from the BJH method, and the curves are shown in Fig. 4b. The results confirmed the presence of massive nano-sized pores on g-C$_3$N$_4$ sheets in the presence of Ca^{2+} ions in comparison with HAp and g-C$_3$N$_4$ nanosheets.
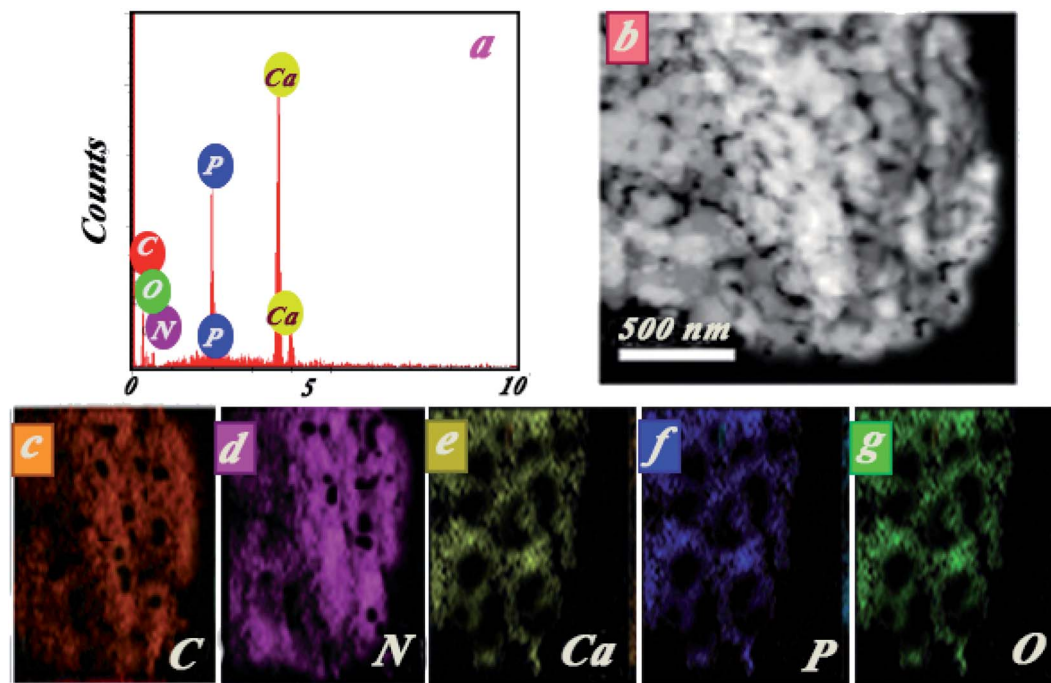
Fig. 3 (a) Initial EDS spectra, (b) selected area for elemental mapping analysis of HAp/g-C_3N_4, (c–g) C, N, Ca, P, and O, respectively.

Except for graphitic carbon nitride, the obtained BET data, especially for the nanocomposite, are remarkably higher than reported by Xu *et al.*[10] For this reason, the fabricated nano-morphology of the composite resulted in enhanced active light harvesting sites favoring a rise in photocatalytic efficiency toward BPA remediation. The holey structure of nanocomposite flattened the active surface area more due to the appearance of numerous holes and edges in the nanosheet planes. Resultant morphology led to the production of a higher pore volume in the nanocomposite in comparison with HAp and g-C_3N_4 nanosheets. Enhanced surface area and pore volume could affect the catalytic activity.

XPS spectra for HAp/g-C_3N_4 compound are shown in Fig. 5. The survey spectra is demonstrated in Fig. 5a, which shows related peaks of O 1s, P 2p, Ca 2p, N 1s, and C 1s for the composite. Orbitals of C 1s in Fig. 5b are located in four positions at binding energies corresponding to N–C=N (289.7 eV), C=O (288.4 eV), C–N (287.6 eV), and C–C (284.6 eV). Two peaks of Ca 2p orbitals appeared at 347.2 and 350.8 eV for Ca $2p_{3/2}$ and Ca $2p_{1/2}$ orbitals, respectively (Fig. 5c). Orbital 2p for the P element was observed at 132.7 eV (see Fig. 5d). Binding energies for C–O and C=O bonds are located at 530.9 and 532.6 eV, respectively (see Fig. 5e). Various bonds between N and C elements are shown in Fig. 5f at binding energies of C–N (398.3 eV), C–N–C (398.7 eV), and N(C)$_3$ (400.7 eV).

As shown in Fig. 6a, XPS survey spectra of both g-C_3N_4 and HAp/g-C_3N_4 contain three peaks at 288, 399, and 532 eV, which can be assigned to C 1s, N 1s, and O 1s signals, respectively. It may be noted that the O 1s weak signal for g-C_3N_4 sample may be originating from adsorbed H_2O on its surface.[40] The molar ratio of C/N elements for HAp/g-C_3N_4 is much smaller than g-C_3N_4, which
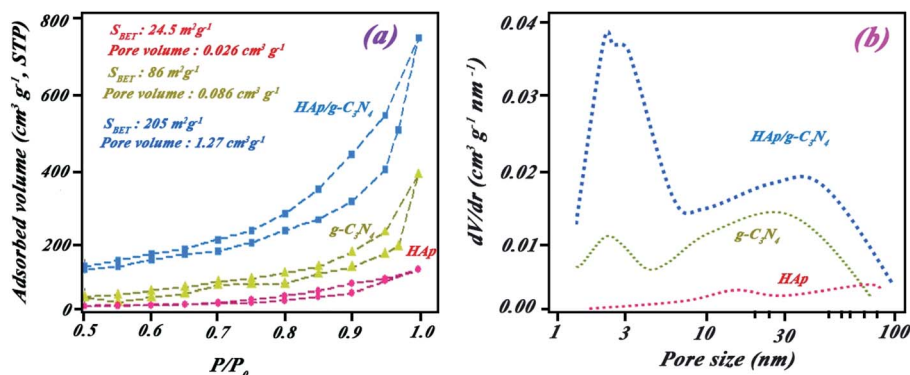

Fig. 4 (a) N_2 adsorption–desorption isotherms for g-C_3N_4 (▲), HAp (●), and HAp/g-C_3N_4 nanocomposite (■) and (b) corresponding BJH pore-size distribution curves.
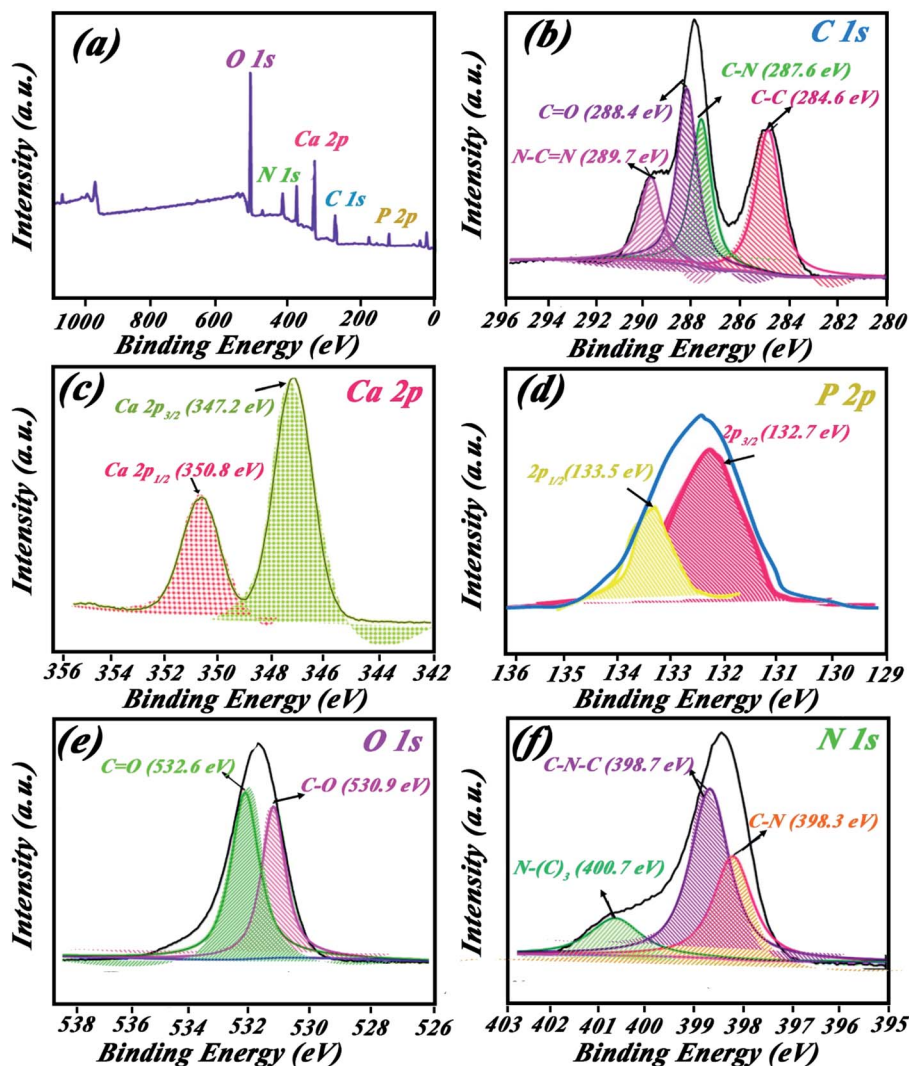
Fig. 5 XPS spectrum (a) survive peaks, (b) C 1s, (c) Ca 2p, (d) P 2p, (e) O 1s, and (f) N 1s orbitals.

suggested the presence of C-vacancies in HAp/g-C$_3$N$_4$. C-vacancies could be related to the reaction of Ca ions with carbonic compounds, forming holey structures.[41] The N 1s spectra are almost the same for both g-C$_3$N$_4$ and HAp/g-C$_3$N$_4$ (Fig. 6b),

indicating that Ca^{2+} ions has little effect on g-C$_3$N$_4$ aromatic systems. But the increasing N 1s peak intensity for HAp/g-C$_3$N$_4$ sample is considered, which can be assigned to N atoms in the vicinity of C-vacancies and obtaining fewer electrons than the
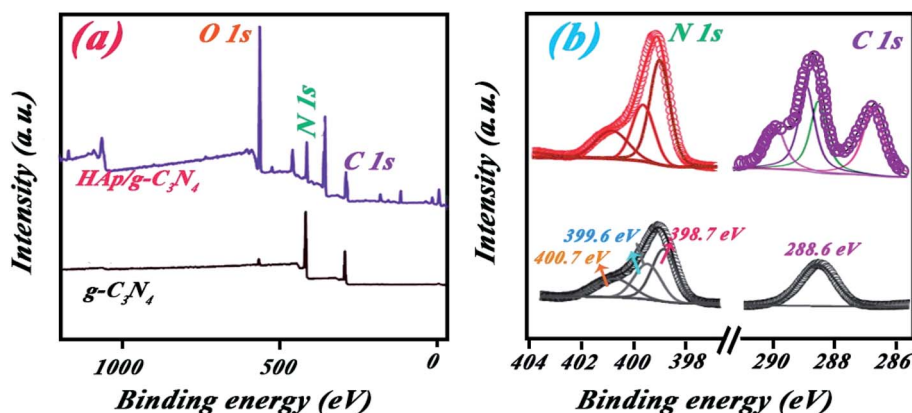

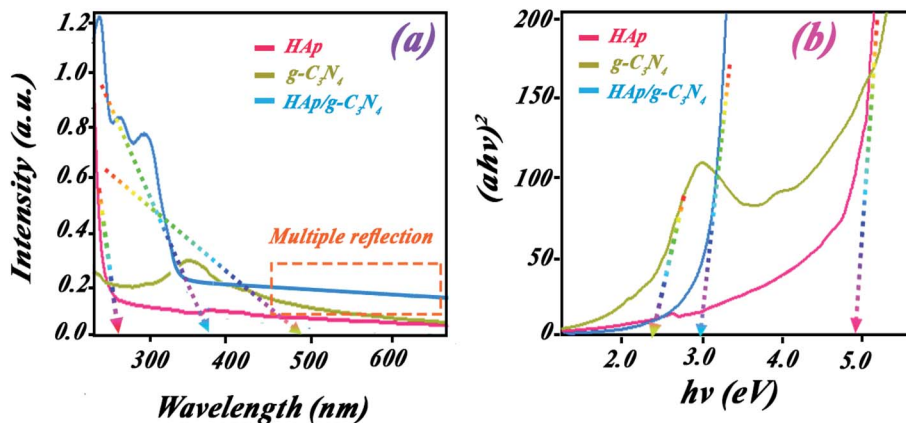Fig. 6 (a) XPS survey spectra and (b) high resolution C 1s and N 1s peaks for g-C$_3$N$_4$ and HAp/g-C$_3$N$_4$.

© 2021 The Author(s). Published by the Royal Society of Chemistry

Fig. 7 UV-visible spectra, (a) and Tauc plots (b) for HAp, g-C$_3$N$_4$, and HAp/g-C$_3$N$_4$.

others. C 1s spectra for both samples are different due to the presence of HAp component in the HAp/g-C$_3$N$_4$ sample. The intensity of C–N in 288.6 eV is higher for the HAp/g-C$_3$N$_4$ sample compared to g-C$_3$N$_4$ sample, which can be attributed to the electron transfer between C-vacancies and N elements. These C-vacancies can enhance the electrical conductivity of the sample and increase the mobility of photoinduced hole–electrons.

3.2. UV-visible spectra

UV-visible studies were done for evaluating the photocatalytic activity of HAp, g-C$_3$N$_4$, and HAp/g-C$_3$N$_4$ nanocomposite. The spectra of HAp nanospheres, nanosheets of g-C$_3$N$_4$, and HAp/g-C$_3$N$_4$ nanocomposite are indicated in Fig. 7a. The HAp nanospheres exhibit a peak in the UV region (<400 nm) with an adsorption edge at 286 nm. For the g-C$_3$N$_4$ nanosheets, a broad peak extended from UV to visible region with an adsorption edge at 435 nm. There is a sharp peak for HAp/g-C$_3$N$_4$ with an adsorption edge (390 nm) between the two adsorptions of HAp and g-C$_3$N$_4$ alone. For the HAp/g-C$_3$N$_4$ composite, a broader tail extended from 540 nm to the near-IR region, which can be attributed to the multiple reflections of light in the existing holes. These results were confirmed by the determination of band gaps of the nanocomposite, Hap, and g-C$_3$N$_4$ by Tauc plot, as shown in Fig. 7b. The calculated band gaps of HAp and g-C$_3$N$_4$ are 3.57 and 2.48 eV, respectively. HAp/g-C$_3$N$_4$ composite has a band gap (2.88 eV) between 3.57 and 2.48 eV. Results suggested that g-C$_3$N$_4$ and nanocomposite are active in the visible light region while HAp does not exhibit any activation in visible light irradiation. Contrary to expectations, the holey structure of HAp/g-C$_3$N$_4$ shows a higher band gap compared to g-C$_3$N$_4$, which can be related to the influence of quantum confinement in the introduced holey structures.[23]

As we know, the most common method to find the band gap from the absorption spectrum is the Tauc method. However, as we used in Fig. 7b, the scattering effect prevents finding a single oblique asymptote.

M–S plots of contents of HAp and g-C$_3$N$_4$ and related nanocomposite HAp/g-C$_3$N$_4$ were established at 1 kHz. It can be noted that all M–S plots have positive slopes, signifying the symbolic n-type character of the semiconductor. The known

eqn (1) for the determination of the type of semiconductor and pertinent flat band potential (V_{fb}) is applied.[42]

$$1/C^2 = \frac{2}{eN_D\varepsilon_0\varepsilon S^2}\left(\left(V - V_{fb}\right) - \frac{KT}{e}\right) \tag{1}$$

where C is the capacitance of interfacial space region, e is the charge of an electron ($e = 1.603 \times 10^{-19}$ C), N_D is the charge density of donor sites in semiconductor (cm^{-3}), ε_0 is the vacuum permittivity ($\varepsilon_0 = 8.854 \times 10^{-14}$ F cm^{-1}), ε is the dielectric constant ($\varepsilon = 5.96$),[43] S stands for activated electrochemical surface area ($S = 1$ cm^2), V shows the amount of applied voltage (V), K is the known Boltzmann constant ($K = 1.381\ 0 \times 10^{-23}$ J K^{-1}), and T is the absolute temperature (°C). The V_{fb} can be estimated by extrapolating the M–S plot to $1/C^2 = 0$, and the values for HAp, g-C$_3$N$_4$, and HAp/g-C$_3$N$_4$ nanocomposite have been obtained as -0.74, -0.55, and -0.93 V (relative to Ag/AgCl), respectively (see Fig. 8a). To explore the carrier transfer, surface potentials of HAp and g-C$_3$N$_4$ semiconductors are estimated by the M–S plots. The potential (Ag/AgCl) was converted to normal hydrogen (NHE) by eqn (2):[44]

$$E_{NHE} = E_{Ag/AgCl} + E^0_{Ag/AgCl} \tag{2}$$

where $E^0_{Ag/AgCl} = 0.197$ V. In particular, for n-type semiconductors, minimum value of conduction band (CB) is 0.1 V higher than flat band potentials.[45] Thus, CB of HAp and g-C$_3$N$_4$ are at -0.643 and -0.453 V (vs. NHE), respectively. Furthermore, band gaps (E_g) of HAp and g-C$_3$N$_4$ are 3.57 and 2.48 eV, respectively, according to Tauc plots. Therefore, using the below eqn (3):[46]

$$E_g = E_{CB} + E_{VB} \tag{3}$$

The position of VB for HAp and g-C$_3$N$_4$ are 2.97 and 2.02 V (vs. NHE).

Moreover, N_D can be determined by eqn (4):

$$N_D = \frac{2}{\varepsilon\varepsilon_{0e_0}}\left[\frac{d\left(\frac{1}{C^2}\right)}{dV}\right]^{-1} = \frac{2}{\varepsilon\varepsilon_{0e_0}}\frac{1}{slop} \tag{4}$$
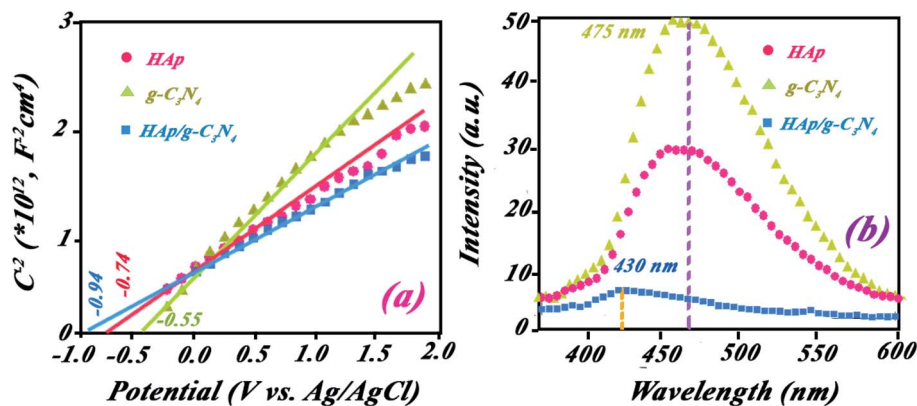
Fig. 8 (a) Mott–Schottky plots for HAp, g-C_3N_4, and HAp/g-C_3N_4 in a 0.5 M Na_2SO_4 aqueous solution. (b) PL spectra for HAp, g-C_3N_4, and HAp/g-C_3N_4 recorded in the excitation wavelength.

The obtained value of N_D for HAp/g-C_3N_4 composite is 3.3×10^{19}, which is higher in comparison with the related values of HAp and g-C_3N_4, which are 2.6×10^{19} and 2.36×10^{19}, showing the shortest and faster charge transport routes for this junction semiconductor with further photocatalytic efficiency. The slope in eqn (4) corresponds to the slope of the M–S plot.

To show the fate of photogenerated hole–electrons in the photocatalytic process, PL spectra were recorded at a suitable excitation wavelength. The sharp peaks of PL with high intensity can be appropriated to the high emission for excited electrons (photogenerated electrons) from conductive band to valence band. Indeed, the low emission of PL spectra indicated the low comeback rate of photoelectrons to the valence band and combination with photogenerated holes. As expected, g-C_3N_4 exhibited high PL intensity while HAp and HAp/g-C_3N_4 have lower intensities (see Fig. 8b). It can be concluded that HAp/g-C_3N_4 indicated a low recombination rate in comparison with the singular phases of HAp and g-C_3N_4. The low recombination rate confirms the high separation of photogenerated holes and electrons, which led to higher photocatalytic efficiency for BPA degradation. Compared to g-C_3N_4, HAp/g-C_3N_4 exhibits a blue shift to lower wavelength emission, which could be assigned to the reported band gaps for these compounds.

3.3. Photocatalytic evolution of HAp/g-C_3N_4 nanocomposite

The photocatalytic activity of the nanocomposite was investigated by photocatalytic degradation of BPA under various conditions. Effective parameters such as photocatalyst amount, solution pH, and concentration of BPA were evaluated to obtain the optimal conditions for high photocatalytic efficiency. Furthermore, the photostability and reusability capability of the nanocomposite were also studied for scale-up aims.

3.3.1. The effect of nanocomposite amounts. Fig. 9a indicates the photocatalytic degradation of BPA (10 ppm) by various photocatalyst amounts under simulated visible light (LED lamp 200 W). Blank experiments (without any photocatalyst) illustrated the low photolysis measured in an amount of 6.7% under light irradiation. In the dark, increasing dye adsorption along with enhancing the photocatalyst amounts confirmed that

more activated adsorption sites are available at higher photocatalyst amounts. Generally, it can be stated that increasing catalyst amount resulted in the higher photocatalytic efficiency due to higher accessible active sites of the applied photocatalyst. Despite the positive influences on catalytic activity, the increasing amount can restrict the photocatalytic efficiency owing to the prevention of visible light diffusion to photocatalyst active sites of highly agglomerated nanopowders in a suspension. However, photocatalyst amount should be optimized within photocatalytic degradation. According to the observed results, 0.01 g of photocatalyst can be introduced as an optimum amount while the efficiency of degradation is permanently reduced for an amount of 0.02 g. Therefore, in order to determine the optimized conditions of other influencing parameters of the photocatalytic process, hereafter, 0.01 g of the photocatalyst was selected as the optimized photocatalyst amount.

3.3.2. The effect of pH value. In order to figure out the effect of pH values on photocatalytic degradation of BPA, different pH values in the range 4–9 were conditioned. According to the depicted results, the surface catalyst HAp/g-C_3N_4 nanocomposite in pH higher than its isoelectric point (6.78) should be negative (see Fig. 2S (ESI file†)). However, BPA molecules at pH 6–8 are positively charged. Hence, at pH 8, the photocatalyst surface with a high negative charge showed higher adsorption of BPA molecules in the dark and subsequently higher photoactivated catalytic degradation of BPA. While, at acidic pH (4 and 5), photocatalyst surface is positively charged but BPA is in anionic form, leading to permanent adsorption of BPA over the photocatalyst surface at these acidic pH values. However, at pH 6, the photocatalyst surface carries a net positive charge and BPA is in the cationic form. Thus, at pH 6, photocatalyst showed lower adsorption along with minor photocatalytic performance in comparison with those at other pH values (see Fig. 9b).

3.3.3. The effect of initial BPA concentration. Initial concentrations of pollutants may have a key role in the adsorption and photocatalytic performance of photocatalyst nanocomposites. Herein, numerous experiments were designed
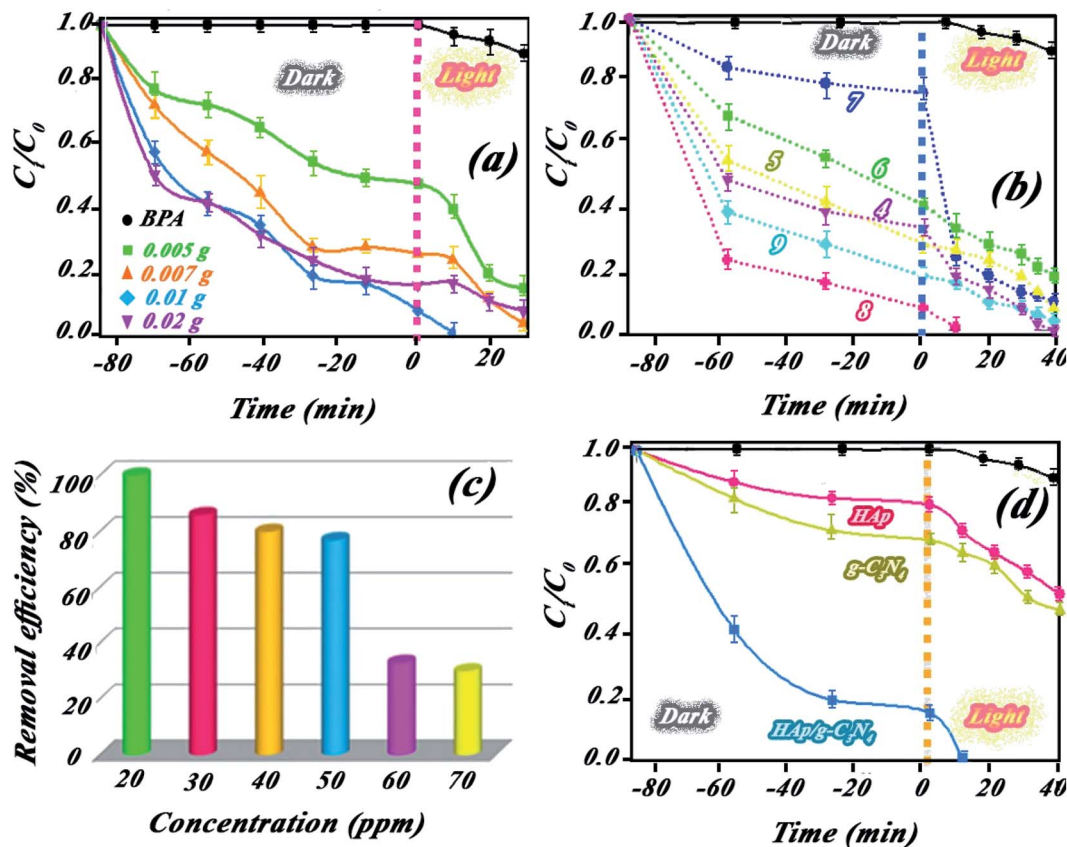
Fig. 9 Photocatalytic activity at (a) different photocatalyst amounts, (b) initial solution pH, (c) various BPA concentrations, and (d) photocatalytic evolution of the composite and its components.

to study the BPA degradation with different concentrations (20–70 ppm) by the synthesized HAp/g-C$_3$N$_4$ nanocomposite. As shown in Fig. 9c, photocatalytic performance reduced with increase in BPA concentrations. The main reason for this behavior is the blocking of active sites of nanocomposites by higher concentrations of BPA. At initial BPA concentrations, surface active sites of the nanocomposite are saturated by polluter molecules that subsequently repel the adsorption of light photons and further photogenerated vibrant radicals.

3.3.4. Photocatalytic performance of the nanocomposite and its components. In this section, the synergetic effect of HAp and g-C$_3$N$_4$ components toward photocatalytic BPA degradation by HAp/g-C$_3$N$_4$ nanocomposite is evaluated. As depicted in Fig. 9d, components of nanocomposite represented a lower degradation capability for BPA compared to the nanocomposite. It can be proposed that photogenerated electrons and holes on the surface of g-C$_3$N$_4$ and HAp should be transferred between these components of the nanocomposite. CB and VB positions, according to M–S calculations, confirmed this observation (see Fig. 8a). Transfer of photogenerated holes and electrons between two components led to the effective separation and reduced recombination of photogenerated charge pairs. In order to evaluate the adsorption amount over the nanocomposite surface, the desorption test was done in an acidic solution at the end of the degradation process. The

amount of pollutant desorption from the nanocomposite surface was measured in very low contents (0.03 ppm), which indicated the degradation process was completed.

3.3.5. Various ratios of HAp/g-C$_3$N$_4$. Another alternative influencing parameter on photocatalytic efficiency of multi-component nanocomposites can be highlighted as the ratio of components. In the present work, using the sol–gel method, different ratios of HAp to g-C$_3$N$_4$ contents were synthesized and applied for degradation of BPA at optimized conditions as discussed above. Photocatalytic efficiencies for 80 : 20, 70 : 30, 60 : 40, 50 : 50, 40 : 60, 30 : 70, and 20 : 80 HAp/g-C$_3$H$_4$ ratios are depicted in Fig. 3S (ESI file†). With increasing g-C$_3$N$_4$ component, the color of the prepared nanocomposite in powder form changed from yellowish to dark brown. The ratio of 50 : 50 for the nanocomposite indicated higher catalytic BPA photodegradation compared to the other ratios (*cf.* Fig. 9a). This behavior has been attributed to the effect of HAp concentration to create a holey structure on g-C$_3$N$_4$ nanosheets, which play a key role in photocatalytic performance. It is probable that the presence of HAp in different proportions had a significant effect on the size of the created holes on the g-C$_3$N$_4$ nanosheets.

3.3.6. Mechanistic and reusability evaluation of photocatalytic process. Scavenging experiments were done to find the possible mechanism of photoactivation degradation of BPA by the nanocomposite catalyst. Hence, methanol (hole scavenger),

IPA (OH· radical scavenger), benzoquinone (superoxide scavenger), and NaN_3 (electron scavenger) were applied for this purpose. Illustrated results confirm that OH· radicals play an important role in the photocatalytic process (Fig. 4Sa (ESI file†)). Therefore, the related photocatalytic mechanism can be proposed as depicted in Scheme 3. Under light irradiation, nanocomposite produced photogenerated hole–electrons that form active radicals, which degrade BPA molecules. This mechanism included two probable routes. Route (I) referred to the key effect of morphology of g-C_3N_4 in capturing and multi-scattering of light. Furthermore, holes acted as active sites for adsorption of photogenerated electrons, which suppressed the recombination of photoinduced charge pairs.[24,28] Hole sites (C-vacancies) also trapped oxygen molecules, which led to more active radicals for the photocatalytic process. These holes in the plane could have a significant effect on the adsorption of more pollutant molecules, which enhanced the degradation rate. Route (II) indicated the preparation of an effective heterojunction between HAp and graphitic carbon nitride nanosheets for photocatalytic degradation of BPA. Photogenerated holes have two options, one could be transferred from the VB of HAp to VB of g-C_3N_4 and react with water molecules to produce active radicals that directly react with BPA molecules or indirectly degrade BPA by oxidized water molecules. But transferred photogenerated electrons to the VB of g-C_3N_4 cannot produce active radicals and just can oxide BPA molecules. In fact, active radicals (OH·) can react with pollutant molecules and in turn oxidize them (follow the proposed mechanism in Scheme 3). Intrinsic O-vacancies of HAp acted as adsorption sites of photogenerated electrons on g-C_3N_4, which led to a high separation of charge carriers. Reusability and stability of the nanocomposite were investigated by the successive photocatalytic process of BPA to assess the usability of nanocomposite in scale-up applications. The operational procedure of the reusability test includes collection of the nanocomposite powder by centrifuge after each catalytic experiment, washing, and drying for reusing.[47–49] The obtained results showed that photocatalytic nanopowder composite has high catalytic performance even after 5 runs (see Fig. 4Sb (ESI file†)). A slight decrease in catalytic efficiency after successive runs can be attributed to losing a low initial amount of the photocatalyst (0.01 g) during the recollection and washing steps.[50–52]

The photocatalytic performance of the nanocomposite was investigated for other pollutants, such as dyes (MB or RhB) and pharmaceutical (diclofenac) pollutants. Indicated results in Fig. 4Sc (ESI file†) suggested the high performance of the nanocomposite for other pollutants. XPS survey of nanocomposite before and after use illustrated in Fig. 4Sd (ESI file†) confirmed high stability of the nanocomposite in successive runs. Scavenging studies in Fig. 3Sa† indicated that hydroxyl radicals are mainly responsible for the photocatalytic degradation of pollutants. Produced hydroxyl radicals were measured by luminescence emission of 2-hydroxyterephthalic acid complex obtained from the reaction of OH· radicals with terephthalic acid (as probe). As shown in Fig. 10a, HAp/g-C_3N_4 produces more OH· radicals due to enhanced PL emission through 20 min illumination. For comparison study, OH· radicals from HAp, g-C_3N_4, and HAp/g-C_3N_4 were measured and plotted in Fig. 10b. It can be seen that HAp/g-C_3N_4 illustrated a higher amount of OH· radical in comparison with HAp and g-C_3N_4.[25,26] ESR analysis also confirmed the production of more OH· radicals by HAp/g-C_3N_4. Other works have also shown that the g-C_3N_4 nanocomposite produced more oxygen radicals under light irradiation in comparison to single g-C_3N_4.[53] Generally, it can be highlighted that carbon-based materials, such as g-C_3N_4 or carbon nanotubes could influence the production of more active radicals due to spatial separation of photogenerated charges.[54,55]

Electron paramagnetic resonance (EPR) analysis at room temperature indicated that the holey structure bears heavily delocalized electrons, which led to a high separation of photo-induced charge pairs. Fig. 10d shows that HAp/g-C_3N_4 exhibited one single Lorentzian line with a g value of 2.004 in the specific range of magnetic field due to lone electrons on the carbon atoms of heptazine rings. Higher intensity EPR for HAp/g-C_3N_4 suggested that a higher number of unpaired electrons improves the production of active radicals. These C-vacancies could act as active sites for the adsorption of photogenerated electrons, oxygen gas, and pollutant molecules.

3.4. Optical characterization

As discussed in Section 3.2 and depicted in Fig. 7, the plotted absorption spectrum of HAp/g-C_3N_4 shows no absorption peak, with a descending curve and its band gap energy can be measured by the Tauc equation.[35] In the z-scan experiments, a colloidal dispersion of the particles in water was prepared and was poured in a 1 mm quartz cell. A He–Ne laser beam with 5 mW output power ($\lambda = 632.8$ nm) was focused with the radius of the beam waist of 45 microns.
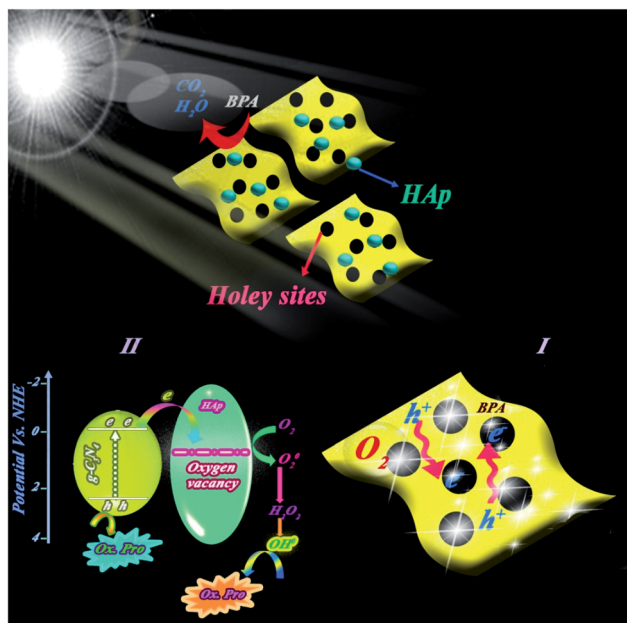
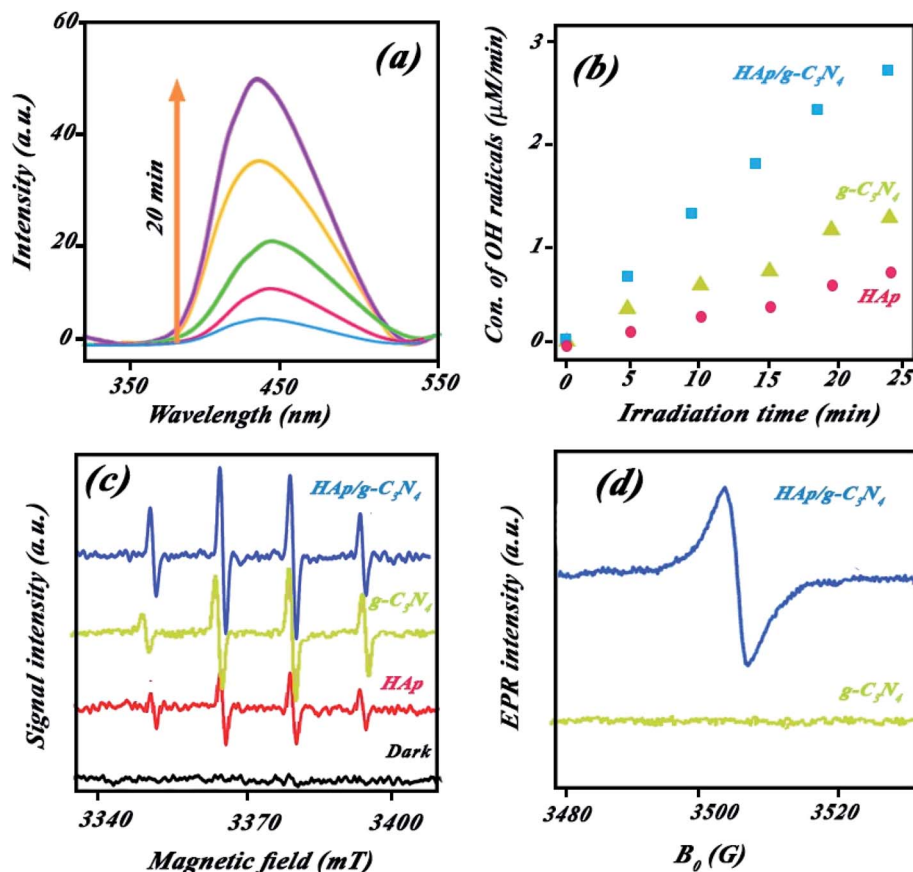Scheme 3 Proposed photocatalytic mechanism of BPA degradation by HAp/g-C_3N_4 nanocomposite.

Fig. 10   (a) PL signal of 2-hydroxyterephthalic acid complex from HAp/g-C$_3$N$_4$, (b) concentration of OH$^\bullet$ radicals from HAp, g-C$_3$N$_4$, and HAp/g-C$_3$N$_4$, (c) resultant EPR signal for OH radicals from HAp, g-C$_3$N$_4$, and HAp/g-C$_3$N$_4$, and (d) EPR spectra for g-C$_3$N$_4$ and HAp/g-C$_3$N$_4$.

This refractive index of the sample would be

$$n = n_0 + \Delta n = n_0 + n_2 I \qquad (5)$$

where I is the incident laser intensity. The change in refractive index Δn is attributed to the intensity of the laser beam and could be considered as a nonlinear term.

The electric field of the passing laser beam at the exit plane of the sample could be written as:[56]

$$E(r,z) = E_0 \frac{w_0}{w(z)} \exp\left(-i\left(kz - \arctan\left(\frac{z}{z_0}\right) \right) \right)$$

$$\exp\left(\frac{-ikr^2}{2R(z)} - \frac{r^2}{w^2(z)} - i\Delta\phi(z,r) - \frac{\alpha L}{2} \right) \qquad (6)$$

where r, w_0, $w(z)$, k, z_0, $R(z)$, α and L are the radial coordinate, the beam waist radius, the beam radius at z, the wave number, the diffraction length of the beam, the radius of the wave front at z, and the absorption coefficient and the sample length, respectively. $\Delta\varphi(z, r)$ is the phase change in the sample due to nonlinear refraction and is given by:

$$\Delta\varphi(z,r) = \frac{kn_2 I_0 L_{\text{eff}}}{1 + \left(\frac{z}{z_0}\right)^2} \exp\left(-2r^2/w^2(z) \right) \qquad (7)$$

and $L_{\text{eff}} = (1 + e^{-\alpha L})/\alpha$, and I_0 are the sample effective length, nonlinear refractive index, and the intensity at the center of beam waist of the beam, respectively. The electric field in the far-field can be obtained using the Fresnel–Kirchhoff diffraction integral at the Fraunhofer approximation, and a theoretical route to achieving the transmitted power through the aperture is briefly explained in previous works.[37] The transmitted power through the aperture can be simply calculated by:[14]

$$P(z) = \int_0^{r_a} I(\rho, z) 2\pi\rho \, d\rho \qquad (8)$$

where r_a is the aperture radius. The normalized transmittance could be calculated using:[14]

$$T(z) = \frac{\int_0^\infty P_T(z, \Delta\varphi_0(t)) \, dt}{\int_0^\infty P_T(z, \Delta\varphi_0 = 0) \, dt}. \qquad (9)$$

This quantity is highly dependent on n_2 and this value can be precisely determined by fitting the experimental curve of the close aperture curve to the theoretical one. Close aperture experiments have been performed, and results are plotted in Fig. 11a. As shown, the peak-valley configuration indicates that the self-defocusing effect ($n < 20$) is the main nonlinear refractive phenomenon. Using the numerical curve fitting by the mentioned equations, the value of the nonlinear refractive
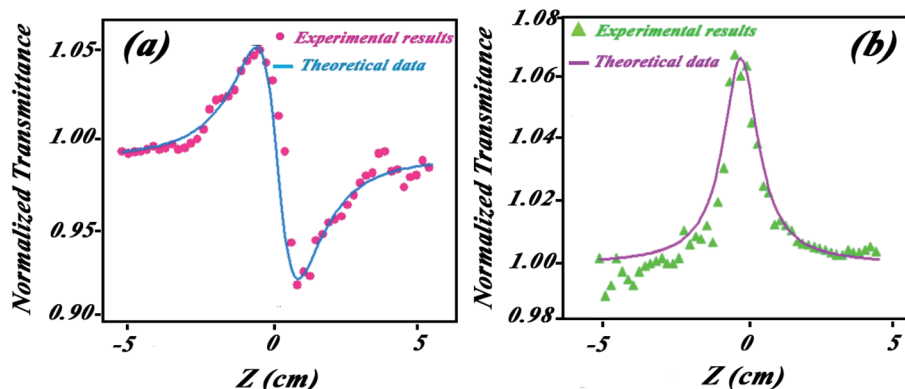
Fig. 11 (a) Theoretical fitted curve (reference) and experimental data of (a) close and (b) open aperture z-scan.

index is obtained as $n_2 = -1.8 \times 10^{-7}$ cm^2 W^{-1}. In low laser radiations, this phenomenon is mainly due to the thermal lensing effect.[56,57] The fitted normalized curve to the average of measurement for the solution has been plotted in Fig. 11b. By opening the aperture, the open aperture curve is obtained that gives nonlinear absorption coefficient β by numerical curve fitting. Theoretical and numerical methods have been discussed in detailes by Alikhani *et al.*[56] The value of nonlinear absorption coefficients has been obtained $\beta = -7.3 \times 10^{-3}$ cm W^{-1} by numerical curve fitting and theoretical relations. The peak configuration of the open aperture curve indicates that the main nonlinear optical phenomenon is the saturation in absorption.[34] As we know, when the light is absorbed by an ensemble of atoms (molecules), the light will force the atoms (molecules) to undergo the transition $2 \rightarrow 1$. Increasing the intensity of the light enhances the population of level 2 until the population inversion occurs. An active material undergoes this population inversion. The threshold beam intensity that can provide the population inversion is called the saturation intensity.[58] In z-scan experiments, the values of saturation intensity can be obtained by the equation:[34]

$$I_s = -\alpha_0/\beta. \qquad (10)$$

The saturation intensity of the synthesized HAP/g-C$_3$N$_4$ NPs is obtained as $I_s = 96$ cm^2 W^{-1} which is lower than the saturation intensity of alumina and ZnO NPs,[34] indicating that these NPs can be suitable for light amplifier devices.

4.   Conclusion

In conclusion, for the first time, holey g-C$_3$N$_4$ nanosheets with numerous carbon vacancies decorated by HAp nanospheres were synthesized through *in situ* sol–gel approach. The presence of Ca^{2+} ions in the initial precursors led to the formation of in-plane hole sites on the g-C$_3$N$_4$ nanosheets. On the other hand, the existence of nitrogen gas during the calcination process of HAp created a desirable platform for the exfoliation of nanosheets from the bulk form. The as-prepared holey structure HAp/g-C$_3$N$_4$ delivers high photocatalytic performance for BPA,

a resistant pollutant. Synthesized HAp/g-C$_3$N$_4$ shows a high surface area of about 205 m^2 g^{-1} and a highly porous structure compared to the non-holey g-C$_3$N$_4$ nanosheets. This work not only proposes an intelligent approach for the holey structure of g-C$_3$N$_4$ but also provides a strategy for the synthesis of hetero-junctions between two effective components of HAp and g-C$_3$N$_4$ nanosheets. Excellent photocatalytic performance is attributed to a variety of material features, such as high surface area, heterojunction between two components, shortening path length, and enhancing the lifetime of charge carriers. Holey structure of nanosheets plays several effective roles: trapping and multiscattering of light, adsorption of photogenerated electrons, adsorption of more pollutant molecules. This newly reported photocatalyst has a high capability for large-scale photocatalytic processes due to its eco-friendly characteristics and biodegradability. Moreover, the measured saturation intensity of this nanocomposite *via* z-scan experiments showed a lower value in comparison with well-known NPs of ZnO and alumina, enabling this new HAp/g-C$_3$N$_4$ nanocomposite as a suitable candidate for use in light amplifier devices.

Conflicts of interest

The authors declare that there is no conflict of interest.

Acknowledgements

References

1 D. Fine, A. Grattoni, R. Goodall, S. S. Bansal, C. Chiappini, S. Hosali, A. L. van de Ven, S. Srinivasan, X. Liu, B. Godin, L. Brousseau, I. K. Yazdi, J. Fernandez-Moure, E. Tasciotti, H. J. Wu, Y. Hu, S. Klemm and M. Ferrari, *Adv. Healthcare Mater.*, 2013, **2**, 632–666.
2 K. Kang, Y. Cho and K. J. Yu, *Micromachines*, 2018, **9**(6), 263–285.

3 A. Bashar Bhuiyan, M. B. Mokhtar, M. E. Toriman, M. B. Gasim, G. C. Ta, R. Elfithri and M. R. Razman, *Am.-Eurasian J. Sustain. Agric.*, 2013, **7**, 126–136.

4 F. N. Chaudhry and M. F. Malik, *J. Ecosyst. Ecography*, 2017, **07**, 111–118.

5 A. K. Dwivedi, *International Research Journal of Mathematics, Engineering and IT*, 2017, **4**, 34–42.

6 M. Hu, Y. Liu, Z. Yao, L. Ma and X. Wang, *Front. Environ. Sci. Eng.*, 2018, **12**, 18.

7 F. Opoku, K. K. Govender, C. G. C. E. van Sittert and P. P. Govender, *Adv. Sustainable Syst.*, 2017, **1**, 1700006.

8 M. E. Simonsen, *Chemistry of Advanced Environmental Purification Processes of Water: Fundamentals and Applications*, 2014, 135–170.

9 M. Chahkandi and M. Zargazi, *J. Hazard. Mater.*, 2020, **389**, 121850.

10 T. Xu, R. Zuo, X. Lei, X. Qi, Q. Wu, W. Yao and Q. Xu, *Appl. Catal., B*, 2019, **245**, 662–671.

11 M. Chahkandi and M. Zargazi, *J. Hazard. Mater.*, 2019, **380**, 120879.

12 M. Zargazi and M. H. Entezari, *Ultrason. Sonochem.*, 2020, **62**, 104867.

13 M. Zargazi and M. H. Entezari, *Ultrason. Sonochem.*, 2020, **67**, 105145.

14 L. Jiang, X. Yuan, G. Zeng, Z. Wu, J. Liang, X. Chen, L. Leng, H. Wang and H. Wang, *Appl. Catal., B*, 2018, **221**, 715–725.

15 L. Jia, X. Cheng, X. Wang, H. Cai, P. He, J. Ma, L. Li, Y. Ding and X. Fan, *Ind. Eng. Chem. Res.*, 2020, **59**, 1065–1072.

16 Z. Jin, Q. Zhang, S. Yuan and T. Ohno, *RSC Adv.*, 2015, **5**, 4026–4029.

17 M. Salimi, A. Esrafili, H. R. Sobhi, M. Behbahani, M. Gholami, M. Farzadkia, A. J. Jafari and R. R. Kalantary, *ChemistrySelect*, 2019, **4**, 10288–10295.

18 X. Li, J. Xiong, J. Huang, Z. Feng and J. Luo, *J. Alloys Compd.*, 2019, **774**, 768–778.

19 R. Shen, J. Xie, H. Zhang, A. Zhang, X. Chen and X. Li, *ACS Sustainable Chem. Eng.*, 2018, **6**, 816–826.

20 X. Bai, L. Wang, R. Zong and Y. Zhu, *J. Phys. Chem. C*, 2013, **117**, 9952–9961.

21 L. R. Zou, G. F. Huang, D. F. Li, J. H. Liu, A. L. Pan and W. Q. Huang, *RSC Adv.*, 2016, **6**, 86688–86694.

22 X. Wu, H. Ma, W. Zhong, J. Fan and H. Yu, *Porous crystalline g-C3N4: Bifunctional NaHCO3 template-mediated synthesis and improved photocatalytic H2-evolution rate*, Elsevier B.V., 2020, vol. 271.

23 Q. Liang, Z. Li, Z. H. Huang, F. Kang and Q. H. Yang, *Adv. Funct. Mater.*, 2015, **25**, 6885–6892.

24 Y. Cao, Z. Xing, Z. Li, X. Wu, M. Hu, X. Yan, Q. Zhu, S. Yang and W. Zhou, *J. Hazard. Mater.*, 2018, **343**, 181–190.

25 F. Yang, H. Li, K. Pan, S. Wang, H. Sun, Y. Xie, Y. Xu, J. Wu and W. Zhou, *Sol. RRL*, 2021, **5**, 2000610.

26 T. Zhao, Z. Xing, Z. Xiu, Z. Li, S. Yang and W. Zhou, *ACS Appl. Mater. Interfaces*, 2019, **11**, 7104–7111.

27 S. Cao, B. Fan, Y. Feng, H. Chen, F. Jiang and X. Wang, *Chem. Eng. J.*, 2018, **353**, 147–156.

28 S. Tan, Z. Xing, J. Zhang, Z. Li, X. Wu, J. Cui, J. Kuang, Q. Zhu and W. Zhou, *J. Catal.*, 2018, **357**, 90–99.

29 V. S. Bystrov, C. Piccirillo, D. M. Tobaldi, P. M. L. Castro, J. Coutinho, S. Kopyl and R. C. Pullar, *Appl. Catal., B*, 2016, **196**, 100–107.

30 M. Sheik-Bahae, A. A. Said, T. H. Wei, D. J. Hagan and E. W. Van Stryland, *IEEE J. Quantum Electron.*, 1990, **26**, 760–769.

31 X. Miao, D. Qu, D. Yang, B. Nie, Y. Zhao, H. Fan and Z. Sun, *Adv. Mater.*, 2018, **30**, 1–8.

32 T. W. Hamann, A. B. F. Martinson, J. W. Elam, M. J. Pellin and J. T. Hupp, *Adv. Mater.*, 2008, **20**, 1560–1564.

33 X. Li, W. C. H. Choy, L. Huo, F. Xie, W. E. I. Sha, B. Ding, X. Guo, Y. Li, J. Hou, J. You and Y. Yang, *Adv. Mater.*, 2012, **24**, 3046–3052.

34 E. Koushki, M. H. Majles Ara and H. Akherat Doost, *Appl. Phys. B: Lasers Opt.*, 2014, **115**, 279–284.

35 Q. Yang, F. Yu, W. Sima and M. Zahn, *AIP Adv.*, 2015, **5**, DOI: 10.1063/1.4931947.

36 M. Gich, A. Roig, C. Frontera, E. Molins, J. Sort, M. Popovici, G. Chouteau, D. Martín y Marero and J. Nogús, *J. Appl. Phys.*, 2005, **98**, DOI: 10.1063/1.1997297.

37 Z. L. I. Iqi, R. L. I. Ang, C. H. I. P. Ang, N. I. D. Ong, J. U. N. W. Ang and H. Aohai, *Opt. Express*, 2019, **27**, 8727–8737.

38 C. L. Popa, M. Albu, C. Bartha, A. Costescu, C. Luculescu, R. Trusca and S. Antohe, *Rom. Rep. Phys.*, 2016, **68**, 1149–1158.

39 L. Berzina-Cimdina and N. Borodajenko, *Infrared Spectrosc.: Mater. Sci., Eng. Technol.*, 2012, DOI: 10.5772/36942.

40 H. Liu, D. Chen, Z. Wang, H. Jing and R. Zhang, *Appl. Catal., B*, 2017, **203**, 300–313.

41 R. P. Panmand, P. Patil, Y. Sethi, S. R. Kadam, M. V. Kulkarni, S. W. Gosavi, N. R. Munirathnam and B. B. Kale, *Nanoscale*, 2017, **9**, 4801–4809.

42 A. Fattah-alhosseini, *Arabian J. Chem.*, 2016, **9**, S1342–S1348.

43 A. K. Dubey and K. I. Kakimoto, *Mater. Sci. Eng., C*, 2016, **63**, 211–221.

44 Y. Surendranath, D. A. Lutterman, Y. Liu and D. G. Nocera, *J. Am. Chem. Soc.*, 2012, **134**, 6326–6336.

45 J. Wang, Y. Yu and L. Zhang, *Appl. Catal., B*, 2013, **136–137**, 112–121.

46 W. Liu, L. Qiao, A. Zhu, Y. Liu and J. Pan, *Appl. Surf. Sci.*, 2017, **426**, 897–905.

47 R. Mohammadi, H. Alamgholiloo, B. Gholipour, S. Rostamnia, S. Khaksar, M. Farajzadeh and M. Shokouhimehr, *J. Photochem. Photobiol., A*, 2020, **402**, 112786.

48 V.-H. Nguyen, M. Mousavi, J. B. Ghasemi, Q. Van Le, S. A. Delbari, A. Sabahi Namini, M. Shahedi Asl, M. Shokouhimehr and M. Mohammadi, *J. Phys. Chem. C*, 2020, **124**, 27519–27528.

49 V. H. Nguyen, M. Mousavi, J. B. Ghasemi, Q. Van Le, S. A. Delbari, M. Shahedi Asl, M. Shokouhimehr, M. Mohammadi, Y. Azizian-Kalandaragh and A. Sabahi Namini, *J. Colloid Interface Sci.*, 2021, **587**, 538–549.

50 V.-H. Nguyen, M. Mousavi, J. B. Ghasemi, Q. Van Le, S. A. Delbari, A. Sabahi Namini, M. Shahedi Asl,

M. Shokouhimehr, H. W. Jang and M. Mohammadi, *Mater. Sci. Semicond. Process.*, 2021, **125**, 105651.

51 V. H. Nguyen, M. Mousavi, J. B. Ghasemi, Q. Van Le, S. A. Delbari, M. Shahedi Asl, M. Mohammadi, M. Shokouhimehr and A. Sabahi Namini, *J. Taiwan Inst. Chem. Eng.*, 2021, **118**, 140–151.

52 H. D. Pham, M. A. Tekalgne, H. H. Do, V. H. Nguyen, D. V. N. Vo, C. K. Cheng, M. Shokouhimehr, C. C. Nguyen, P. Singh, P. Raizada, S. Y. Kim and Q. Van Le, *Mater. Lett.*, 2021, **288**, 129355.

53 Q. Zhang, Y. Peng, Y. Lin, S. Wu, X. Yu and C. Yang, *Chem. Eng. J.*, 2021, **405**, 126661.

54 Y. Lin, C. Yang, S. Wu, X. Li, Y. Chen and W. L. Yang, *Adv. Funct. Mater.*, 2020, **30**, 2002918.

55 Y. Lin, X. Wu, Y. Han, C. Yang, Y. Ma, C. Du, Q. Teng, H. Liu and Y. Zhong, *Appl. Catal., B*, 2019, **258**, 117969.

56 S. Alikhani, H. Tajalli and E. Koushki, *Opt. Commun.*, 2013, **286**, 318–321.

57 E. Koushki, J. Baedi and A. Tasbandi, *J. Electron. Mater.*, 2019, **48**, 1066–1073.

58 O. Svelto, *Energy Levels, Radiative and Nonradiative Transitions in Molecules and Semiconductors*, 2010.